

MEASUREMENTS OF X-RAY SCATTERING FROM INTERSTELLAR GRAINS

CHRISTOPHER W. MAUCHE AND PAUL GORENSTEIN

Harvard-Smithsonian Center for Astrophysics

Received 1985 April 9; accepted 1985 September 4

ABSTRACT

We report on the results of an *Einstein Observatory* imaging proportional counter investigation of the halos produced by the scattering of X-rays from interstellar grains of four compact Galactic (low-latitude) and two extragalactic (high-latitude) X-ray sources. We find that the intensity of these halos correlates well with (1) the amount of visual extinction and (2) the distance through the Galaxy's dust layer: quantities which measure the column density of grains to a given source. From this result, and from the size and shape of the halos from the Galactic sources, we are able to derive a number of grain parameters in the context of two alternate grain size distributions: the Mathis-Rumpl-Nordsieck (MRN) and the Oort-van de Hulst distributions, either of which is capable of producing the observed halos. Though no single grain size is capable of producing the shapes observed for these halos, a mean size of $\sim 0.1 \mu\text{m}$ and a number density of $\sim 10^{-12}$ grains cm^{-3} produce the correct halo intensities. From the additional parameters determined from the size and shape of the halos, we find results concerning the amount of material in grains which are in general agreement with the observed depletion of the elements from the gas phase of the interstellar medium, as well as with the detailed predictions of the MRN size distribution.

Subject headings: interstellar: grains — X-rays: sources

I. INTRODUCTION

Over two decades have passed since Overbeck (1965) first drew attention to the possibility of measuring the scattering of X-rays from interstellar grains. In that time, many theoretical papers have been published discussing various properties and consequences of this scattering, though only with the imaging X-ray capabilities of the *Einstein Observatory* (Giacconi *et al.* 1979) have a few observational papers appeared.

Because of this, less than a dozen sources have been examined for the existence of X-ray halos. Rolf (1983) contributed the first with his analysis of an imaging proportional counter (IPC) observation of 4U 1658–48 (GX 339–4), which showed a significant excess above a model of the point response for this source. Positive detections were reported by Catura (1983) as well, in his high resolution imager (HRI) study of LMC X-3 and five Galactic X-ray sources. Though unable to take proper account of LMC X-3, he consistently found 10%–20% halo intensities for the four sources at low Galactic latitude. This compares with the insignificant halo detected for the source at relatively high Galactic latitude, which presumably has a correspondingly low column density of grains as compared to the four sources in the Galactic plane. Most recently, Bode *et al.* (1985) have employed the HRI and a unique method involving the time delay of scattered rays to reveal the X-ray halo of Cyg X-1.

We report on an IPC study of the X-ray halos of four Galactic and two extragalactic X-ray sources complementary to the HRI study undertaken by Catura (1983). We include a reexamination of 4U 1658–48 in light of the results of a detailed study of the IPC's point response function (PRF), as well as another look at GX 13+1, which was among the sources examined by Catura (1983) with the HRI. We employ the IPC for this investigation in spite of its complicated PRF, since its high sensitivity, low background, energy resolution, and wide field of view make this detector the instrument of choice for the measurement of X-ray halos, which are intrinsically extended and low in surface brightness.

The plan of this paper is as follows. In § II we give theoretical expressions for the expected size and intensity of an X-ray halo. This is followed by a detailed discussion of instrumental properties concerning the IPC's energy- and pulse height channel-dependent PRF (§ III), the resulting source PRFs (§ IV), and the measured surface brightness profiles (SBPs) (§ V). These are compared in § VI to reveal the X-ray halos, as well as an important correlation between the strength of these halos and quantities which measure the column density of grains toward each source. We follow this with a discussion concerning the theoretical shape of an X-ray halo (§ VII), which is dependent on the spatial distribution of grains along the line of sight as well as on the assumed grain size distribution (§ VIII). We place constraints on the resulting grain parameters in § IX and close in § X with a summary of our results.

II. THE THEORETICAL SIZE AND STRENGTH OF AN X-RAY HALO

As discussed by van de Hulst (1957), Overbeck (1965), and Hayakawa (1970), the differential and total scattering cross sections in the Rayleigh-Gans approximation for a spherical particle of radius a are given by

$$\frac{d\sigma_{\text{scat}}}{d\Omega} = 2a^2 \left(\frac{2\pi a}{\lambda} \right)^4 |m - 1|^2 \left(\frac{j_1(x)}{x} \right)^2 (1 + \cos^2 \theta_{\text{scat}}), \quad (1)$$

$$\sigma_{\text{scat}} = 2\pi a^2 \left(\frac{2\pi a}{\lambda} \right)^2 |m - 1|^2, \quad (2)$$

where m is the complex index of refraction,

$$x = \left(\frac{4\pi a}{\lambda} \right) \sin \left(\frac{\theta_{\text{scat}}}{2} \right), \quad (3)$$

and $j_1(x)$ is the spherical Bessel function of first order.¹ In the limit of small angles,

$$x \approx \frac{2\pi a}{\lambda} \theta_{\text{scat}}, \quad (4)$$

and $(j_1(x)/x)^2$ is nearly Gaussian:

$$9 \left(\frac{j_1(x)}{x} \right)^2 \approx \exp \left(-\frac{x^2}{2\sigma^2} \right) = \exp \left(-\frac{\theta_{\text{scat}}^2}{2\tilde{\sigma}^2} \right). \quad (5)$$

Matching half-intensity points for these two functions gives

$$\tilde{\sigma} = \frac{10.4}{E(\text{keV})a(0.1 \mu\text{m})} \text{ arcmin}, \quad (6)$$

which indicates the typical size of the halo produced by a single grain of radius a .

The expression for the scattering cross sections can be put in a more useful form by writing

$$|m - 1| = |-\delta + i\beta| = |\delta_\infty| |(f_1 + if_2)/Z|, \quad (7)$$

where

$$\delta_\infty = -\frac{n_e r_e \lambda^2}{2\pi} = -\pi(\hbar c)^2 N_A r_e \left(\frac{2Z}{M} \right) \rho E^{-2} \quad (8)$$

is the high frequency behavior of the real decrement of the complex index of refraction, r_e is the classical electron radius, N_A is Avogadro's number, ρ is the mass density, E is the energy,

$$|f_1 + if_2| = F(E) \quad (9)$$

is the atomic scattering factor (Henke 1981), Z is the atomic charge, and M is its mass number. Then the cross sections take on the more explicit forms

$$\frac{d\sigma_{\text{scat}}}{d\Omega} = 1.1 \times 10^{-6} \left(\frac{2Z}{M} \right)^2 \left(\frac{\rho}{3} \right)^2 a(0.1 \mu\text{m})^6 \left[\frac{F(E)}{Z} \right]^2 \exp \left(-\frac{\theta_{\text{scat}}^2}{2\tilde{\sigma}^2} \right) \text{ cm}^2, \quad (10)$$

$$\sigma_{\text{scat}} = 6.3 \times 10^{-11} \left(\frac{2Z}{M} \right)^2 \left(\frac{\rho}{3} \right)^2 a(0.1 \mu\text{m})^4 E(\text{keV})^{-2} \left[\frac{F(E)}{Z} \right]^2 \text{ cm}^2. \quad (11)$$

This last equation affords us an order of magnitude estimate for the intensity of an X-ray halo.

As discussed by Hayakawa (1970), the image of an X-ray source will consist of a point source core of unscattered photons and a surrounding halo due to X-rays scattered by interstellar grains. These have intensities

$$I_{\text{Core}} = I \exp(-\sigma_{\text{scat}} n_g d), \quad (12)$$

$$I_{\text{Halo}} = I[1 - \exp(-\sigma_{\text{scat}} n_g d)], \quad (13)$$

where $n_g d = N_g$ is the column density of grains between the source and the observer. The fractional intensity of the halo is then

$$\frac{I_{\text{Halo}}}{I_{\text{Halo}} + I_{\text{Core}}} = 1 - \exp(-\sigma_{\text{scat}} n_g d) \approx \sigma_{\text{scat}} n_g d. \quad (14)$$

¹ The Rayleigh-Gans approximation requires

$$\left(\frac{4\pi a}{\lambda} \right) |m - 1| \ll 1,$$

or

$$a \ll 0.16 \left[\left(\frac{2Z}{M} \right) \left(\frac{\rho}{3} \right) \left(\frac{F(E)}{Z} \right) \right]^{-1} E(\text{keV}) \mu\text{m},$$

in light of the definitions in equations (7)–(9). Consequently, we may apply this approximation with impunity to grain sizes $a \lesssim 0.3 \mu\text{m}$, since the mean energy of the sources for which we extract grain parameters is $\sim 2 \text{ keV}$. The accuracy to which the Rayleigh-Gans approximation equals the exact formulation of the scattering cross section is evident in Martin (1970).

Consequently, a measurement of the fraction of the total number of X-rays residing in a source's halo is essentially a direct measure of the quantity $\sigma_{\text{scat}} n_g d$, which is the "optical" depth to the source. Turning this around, the fractional intensity of an X-ray halo is

$$\frac{I_{\text{Halo}}}{I_{\text{Halo}} + I_{\text{Core}}} \approx 0.20 \left(\frac{2Z}{M} \right)^2 \left(\frac{\rho}{3} \right)^2 a(0.1 \mu\text{m})^4 E(\text{keV})^{-2} \left[\frac{F(E)}{Z} \right]^2 \left(\frac{n_g}{10^{-12}} \right) d(\text{kpc}) \approx 0.2d(\text{kpc}). \quad (15)$$

Another estimate of this quantity comes from a comparison with the amount of visual extinction. As discussed by Martin (1970), the "optical depth" to a source at X-ray wavelengths τ_x is related to the optical depth at visual wavelengths by

$$\tau_x = \tau_v Q_{\text{scat}}/Q_{\text{ext}} = \sigma_{\text{scat}} n_g d, \quad (16)$$

where Q_{scat} is the scattering efficiency at X-ray wavelengths,

$$Q_{\text{scat}} = \frac{\sigma_{\text{scat}}}{\pi a^2} = 0.20 \left(\frac{2Z}{M} \right)^2 \left(\frac{\rho}{3} \right)^2 a(0.1 \mu\text{m})^2 E(\text{keV})^{-2} \left[\frac{F(E)}{Z} \right]^2, \quad (17)$$

and $Q_{\text{ext}} \lesssim 2$ is the extinction efficiency at visible wavelengths. Since the optical depth at visual wavelengths $\tau_v = 1.086A_v(\text{mag})$, the fractional halo intensity is

$$\frac{I_{\text{Halo}}}{I_{\text{Halo}} + I_{\text{Core}}} \approx 0.10 \left(\frac{2Z}{M} \right)^2 \left(\frac{\rho}{3} \right)^2 a(0.1 \mu\text{m})^2 E(\text{keV})^{-2} \left[\frac{F(E)}{Z} \right]^2 A_v(\text{mag}) \approx 0.1A_v(\text{mag}). \quad (18)$$

Interestingly, equations (15) and (18) for the halo intensity give

$$A_v(\text{mag}) \approx 2a(0.1 \mu\text{m})^2 \left(\frac{n_g}{10^{-12}} \right) d(\text{kpc}), \quad (19)$$

which is the observational "law" of ~ 2 mag of visual extinction per kiloparsec. This equation indicates that a $(0.1 \mu\text{m})^2(n_g/10^{-12})$ must be of the order of one.

Two important caveats must be made concerning these results:

a) *The energy dependence of the scattering cross section.*—The first point concerns the effect of the energy dependence of the scattering cross section. This energy dependence has the effect of producing variations in the "optical" depth to, and consequently the halo intensity of, a given source due solely to variations in its X-ray spectrum. Similarly, a hypothetical group of sources differing only in their X-ray spectra will present halos of differing intensities—sources with softer spectra having brighter X-ray halos, and vice versa. The spectra of these sources will differ not only because of intrinsic spectral differences, but because of differing amounts of absorption by interstellar gas and dust, which acts to remove low-energy X-rays from a source's intrinsic spectrum. Consequently, this absorption has the effect of producing harder X-ray spectra (and consequently weaker X-ray halos) for distant sources than they would have had in the absence of interstellar absorption. We can account for these effects by noting the effective energy of each source, and with this correct the observed values of $\sigma_{\text{scat}} n_g d$ to their values at 1 keV. In light of equation (11), these are equal to $\sigma_{\text{scat}} n_g d \langle E^* \rangle^2$, where $\langle E^* \rangle$ is the effective energy.

b) *Source Variability.*—Another important point concerns the application of equations (15) and (18). The initial relations leading to these equations implicitly assumed that the source under examination was in a constant intensity state for a length of the time *previous* to the observation. This is due to assumption (13) and to the time delay for rays in the halo compared to rays which travel directly from the source to the observer. Because of this time delay, the halo intensity will depend in a complicated way on the source intensity previous to an observation over a length of time of order of the maximum time delay experienced by scattered rays. Consider, for example, rays which are deflected through an angle equal to the angular width of the differential scattering cross section ($\sim 10'$). The relative extra distance traveled by the scattered ray is negligibly small: $\Delta d/d \lesssim 1 \times 10^{-6}$. However, because of the great distances involved, the associated time delay can be considerable:

$$\Delta t \lesssim 1 \times 10^{-6}(d/c) \approx 1 \times 10^5 d(\text{kpc}) s \approx 1.3d(\text{kpc}) \text{ days}, \quad (20)$$

where $d(\text{kpc})$ is the distance through the Galaxy's dust layer in kiloparsecs.

Some interesting consequences of the delay of scattered rays have been considered by Trümper and Schönfelder (1973), Spiegler and Trümper (1975), Alcock and Hatchett (1978), and Bode *et al.* (1985). What concerns us here is the application of equation (13) and the resulting validity of equations (15) and (18) for each of our sources. Unfortunately, this is the most troublesome for the most distant sources—the very sources in our sample which are the most variable. These sources are 4U 1658–48, GX 13+1, and Cyg X-3, and their associated characteristic delays are ~ 2 , 7, and 13 days respectively. It is not known how the intensity of any of these sources varied during these intervals—only GX 13+1 was observed for any length of time (~ 3 days, or $\sim 0.4\Delta t$) previous to our observation. During this time its intensity was essentially constant. Cyg X-3, on the other hand, is known to vary in intensity by a factor of ~ 2 over its 4.8 hr period. In order to account for this variation, we included data taken during roughly equal intervals separated by $\sim (\text{integer} + \frac{1}{2})$ times 4.8 hr, which assures that we observed Cyg X-3 in a time-average state over its period. Whether this accounts for its long-term variability is, however, unknown, though we note that the mean intensity of this source is relatively stable over periods of up to twice the length of the characteristic delay of its scattered rays (see van der Klis and Bonnet-Bidau 1983).

III. THE POINT RESPONSE FUNCTION

The search for extended structure of any kind must be made with a clear understanding of the measured point response function (PRF) of the instrument employed in the investigation. The PRFs for the instruments of the *Einstein Observatory* were determined during calibration testing at Marshall Space Flight Center prior to the observatory's launch. Each PRF is the result of contributions from the intrinsic spatial resolution of the individual detectors and the point response of the image-forming mirror elements.

At 0.5 per resolution element, the HRI has a spatial resolution fine enough to directly sample the mirror's point response, which is known to be a function of both energy and off-axis angle. Only the energy dependence will concern us here, since all the sources discussed in this paper were on-axis observations. The energy dependence of the mirror's point response was determined during testing of the HRI/mirror combination with ten energies, ranging from 0.2 to 4.5 keV. The resulting calibration images completely define the point response of the mirror. Figure 1a shows the surface brightness distribution for a few of the many energies for which calibration data were taken with the HRI. The profiles have prominent wings due to scattering from surface imperfections in the mirror elements, an effect which increases dramatically with increasing energy. These mirror-scattering wings must, of course, be present in the corresponding IPC profiles, since the HRI profiles simply measure the point response of the mirror.

The IPC/mirror combination was tested at five energies and three high-voltage settings. An initial study of this body of data revealed a PRF with a pulse height channel-dependent Gaussian core and energy-dependent power-law wings. This is to be understood as the convolution of the IPC's intrinsic spatial resolution, which is pulse height channel-dependent and nearly Gaussian, and the mirror's nearly power law point response. Figure 1b shows the surface brightness profile for the two extreme energies for which the IPC was calibrated. The 0.3 keV profile is dominated by its broad core, whereas the 4.5 keV profile has a much narrower core and prominent wings. Intermediate energies, of which there are three, present intermediate profiles with respect to both the width of the core and the contribution of scattering from the mirror elements.

This information has served up to the present time to define the PRF of the IPC/mirror combination. For the purposes of this investigation, however, we felt it necessary to reexamine these data and those of the HRI/mirror combination to better understand the surface brightness profiles of arbitrary celestial sources observed with the IPC. This work was guided by the philosophy

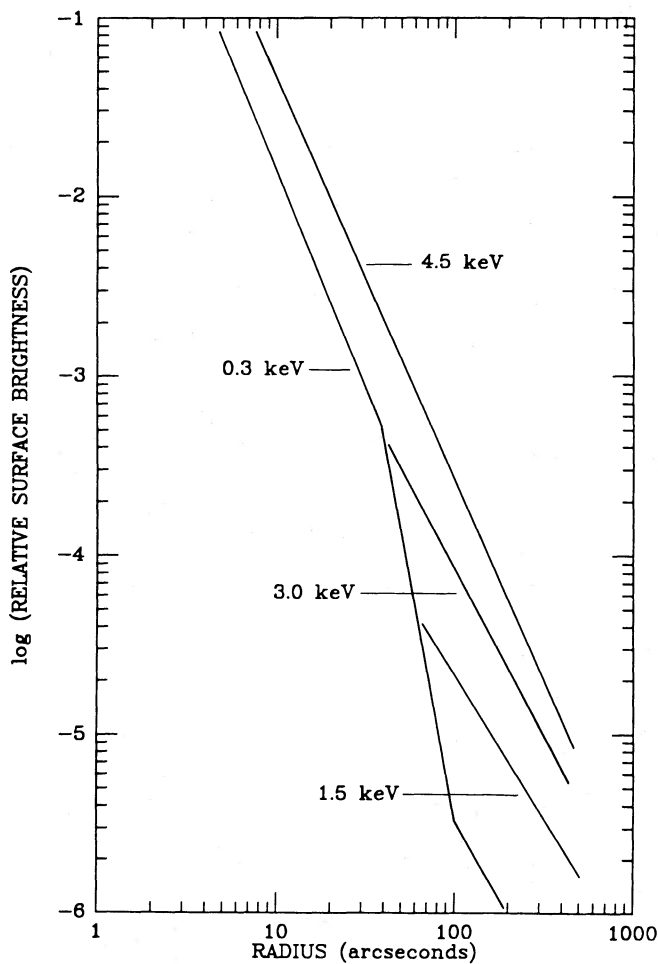


FIG. 1a

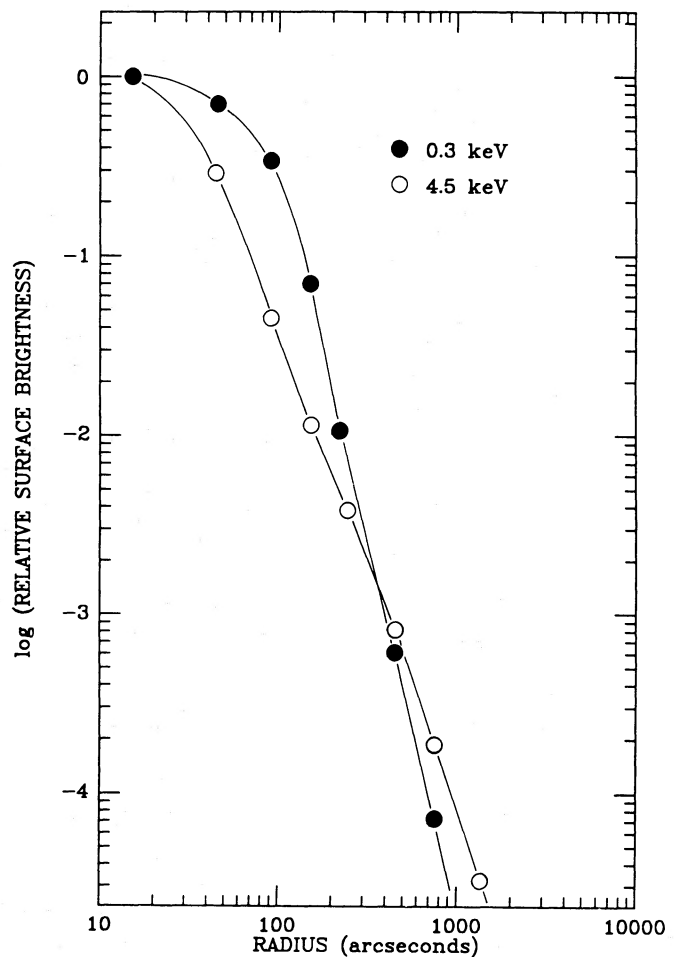


FIG. 1b

FIG. 1.—Schematic representation of a subset of the point-source calibration data taken for (a) the HRI and (b) the IPC. The response of the IPC is the convolution of its intrinsic (Gaussian) spatial resolution with the point response of the mirrors.

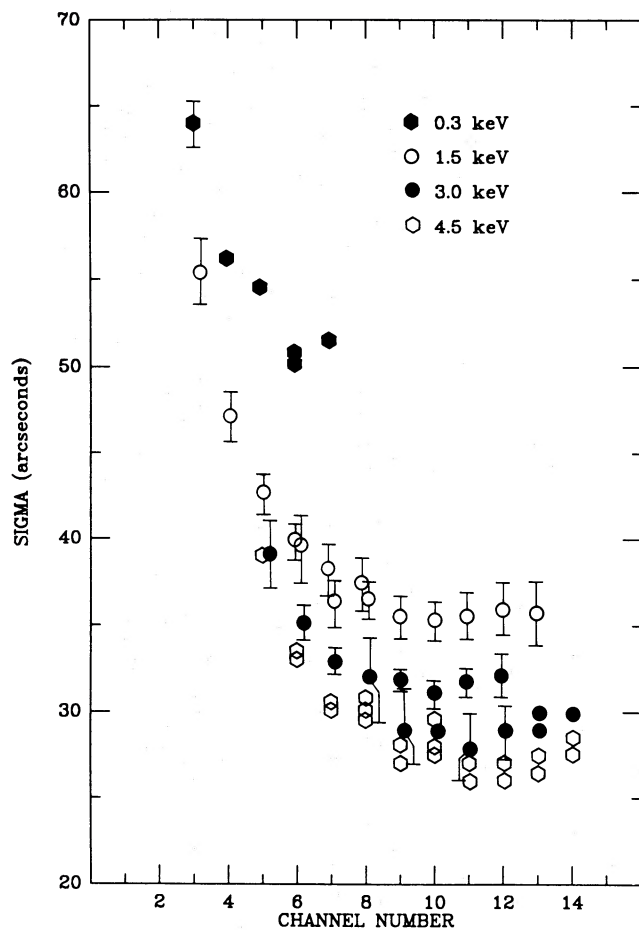


FIG. 2a

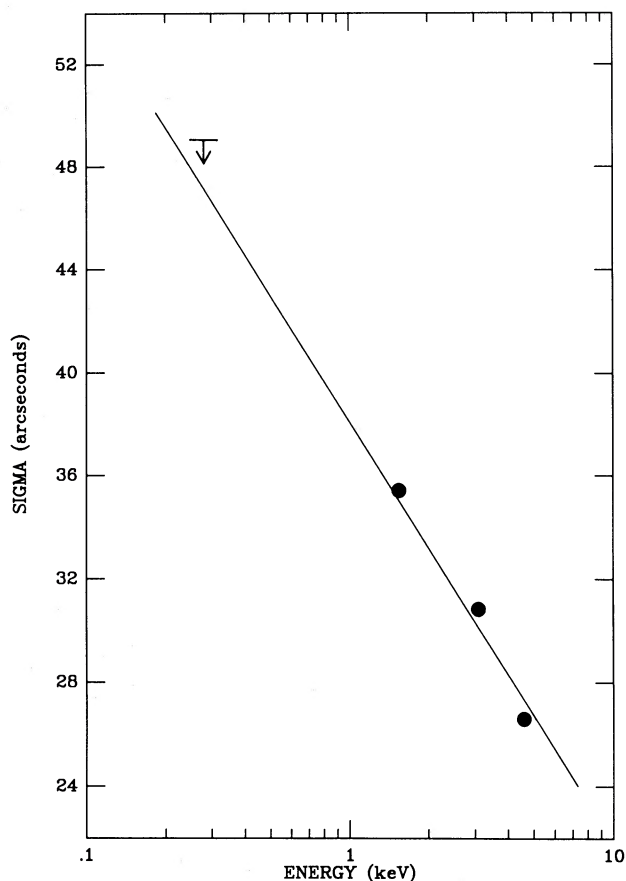


FIG. 2b

FIG. 2.—(a) The Gaussian width of the IPC spatial resolution as a function of pulse height channel for four energies spanning the *Einstein* bandpass. (b) The asymptotic (minimum) value of the IPC's spatial resolution as a function of energy from (a).

described above: the IPC/mirror PRF will be the convolution of the IPC's intrinsic spatial resolution (which is Gaussian and channel-dependent) and the mirror's point response (which is measured by the HRI and is energy-dependent). In this way, it should be possible to convolve a single HRI calibration image with 15 different Gaussian widths to produce each of the 15 channels that comprise an IPC calibration image. This procedure can be repeated for each of the five energies for which calibration data is common to the two instruments.

It is sometimes also possible to compare model profiles to a number of measured single-channel IPC PRFs, since data exist for each energy at three high-voltage settings. In this way, a number of independently determined assessments may be made of the Gaussian widths. This information, which quantifies the IPC's spatial resolution, is presented in Figure 2a. A formal error assessment is not always possible, but the error bars shown are $\sim 90\%$ confidence (Lampton, Margon, and Bowyer 1976). A number of trends are apparent from this figure. First and most obviously is the channel dependence of the IPC's spatial resolution. Superposed on this is a more subtle energy dependence, a trend observable in the measured IPC calibration data and quantified by our fitting procedure. There is also some indication of a gain dependence in the sense that the spatial resolution increases with increasingly high voltage. We shall average through this marginally significant variation.

The last trend apparent in the IPC's spatial resolution is indicated in Figure 2b. The curves in Figure 2a flatten out for each energy to some minimum value. This minimum or asymptotic spatial resolution is plotted against energy in Figure 2b. The trend is consistent with an inversely linear dependence on the log of the corresponding energies. With this graph and the family of curves of Figure 2a, it is possible to predict the IPC's spatial resolution at a given channel for an arbitrary energy between 0.3 and 4.5 keV.

In particular, it is possible to closely determine the IPC's spatial resolution at 0.6, 0.7, 0.9, and 2.0 keV—the extra energies for which the HRI was calibrated and, consequently, for which the response of the mirror is known. With this information, we have the potential for a library of 135 separate model IPC PRFs (at nine energies in 15 channels). We have settled, however, for a library of 81 entries, since the spatial resolution for a given energy is essentially the same in the last five channels and is too poor to be of any use in the first two channels. This leaves nine unique channels at nine energies between 0.3 and 4.5 keV. This profusion of data allows us to accurately model the PRF of the IPC for an arbitrary source spectrum and high-voltage setting, just as they successfully reproduce the measured profiles of the IPC's calibration data.

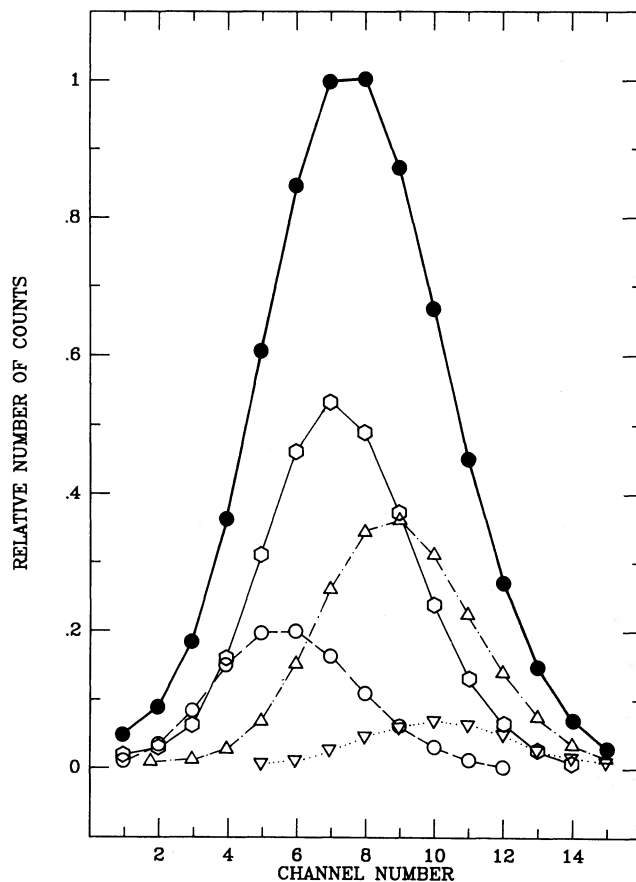


FIG. 3.—The decomposition of the pulse height distribution (*filled circles*) for 4U 1658–48 into separate distributions arising from the four major regions of its spectrum centered at 0.9 (*open circles*), 1.5 (*hexagons*), 2.0 (*triangles*), and 3.0 (*inverted triangles*) keV (peaking left to right). This information determines the fractional contribution of each of these energies to each pulse height channel in the model PRF.

IV. THE MODEL POINT RESPONSE FUNCTIONS

The procedure for modeling the PRF of real sources involves a determination of each source's incident spectrum. This is done for the IPC in the usual manner of proportional counter data: model spectra are convolved with the instrument response to produce a distribution of counts across the pulse height channels. This model distribution is compared to the measured distribution as the free parameters in the spectral function are varied. In this way, an acceptable spectral representation is found which accurately reproduces the measured pulse height distribution.

In the context of our library of PRFs, this resulting pulse height distribution is the superposition of a number of separate pulse height distributions, each rising from the response of the detector to a different region of the spectrum. This concept is illustrated in Figure 3 for the case of 4U 1658–48. Since our library characterizes the PRF for each channel at the nine energies 0.3, 0.6, 0.7, 0.9, 1.5, 2.0, 3.0, 3.4, and 4.5 keV, we treat separately the regions of the spectrum which contain these energies. These are designated according to the element whose X-ray fluorescent line appears in the band: carbon 0.05–0.4 keV; chromium, 0.4–0.6 keV; iron, 0.6–0.8 keV; copper, 0.8–1.2 keV; aluminum, 1.2–1.8 keV; zirconium, 1.8–2.5 keV; silver, 2.5–3.2 keV; tin, 3.2–4.0 keV; and titanium, 4.0–6.4 keV. Only a minor modification to the standard spectral analysis program is necessary to obtain the predicted response for the detector to each of these energy bands separately. This information determines the fractional contribution of each of the nine energies to each pulse height channel. In this way, the 81 PRF arrays may be weighted to produce the PRF for an arbitrary source spectrum. Note that this procedure treats the form of the spectrum exactly, while approximating the energy dependence of the PRF by its measured form at nine discrete energies.

The best-fit spectral parameters for the six sources included in this study appear together in Table 1. The first source, 3C 273, was best fitted with a power-law spectrum (dN/dE) of slope $\alpha = 1.40$, a result consistent with previous measurements. The form of the spectrum for the next four sources could be represented equally well by either a power-law or a thermal bremsstrahlung spectrum. We present the best-fit parameters for each type of spectrum for each of these four sources. The form of the spectrum for the last source, Cyg X-3, had to be determined by the monitor proportional counter (MPC), due to this source's high temperature and strong low-energy cutoff. The value of N_H was obtained by the IPC given the spectral form supplied by the MPC. This procedure makes the most of the characteristics of each of these instruments in the determination of this source's spectrum.²

² It should be stressed that the spectra found by the IPC were checked against the MPC spectra for all the sources, and that consistent results were obtained by the two instruments.

TABLE 1
SOURCE SPECTRA

Source	Sequence Number	Spectral Type ^a	Index ^b	N_{H} (cm^{-2})
3C 273	I9310	Power law	1.4	6.8×10^{19}
LMC X-1	I6516	Power law	3.3	1.5×10^{22}
		Thermal bremsstrahlung	1.4	1.3×10^{22}
4U 1254-69	I6614	Power law	1.8	5.0×10^{21}
		Thermal bremsstrahlung	6.7	4.3×10^{21}
4U 1658-48	I1042	Power law	4.1	1.6×10^{22}
		Thermal bremsstrahlung	0.9	1.2×10^{22}
GX 13+1	I8133	Power law	1.2	4.9×10^{22}
		Thermal bremsstrahlung	5.1	4.6×10^{22}
Cyg X-3	I3378	Blackbody	6.1	3.2×10^{22}

^a dN/dE .

^b Temperature in keV for thermal bremsstrahlung and blackbody spectra; power-law (number) index ($E^{-\alpha}$) for power-law spectra.

We used these spectral forms to construct model PRFs for each source in the manner previously described. Two profiles were constructed for each of the four sources which have two spectral forms appearing in Table 1. This duality allows a check of the sensitivity of the form of the model PRFs to the exact form of the source spectrum. We found no difference between the model PRFs for each spectral form for each of these four sources. Consequently, we expect little error to arise from using the best-fit spectral parameters in Table 1 to construct model PRFs for each source.

V. THE MEASURED SURFACE BRIGHTNESS PROFILES

Having constructed a model PRF for each of our sources, a comparison may be made between these model profiles and each source's measured surface brightness profile (SBP) to search for extended structure. In light of the energy dependence of the X-ray scattering cross section, we account separately for the SBP in three bands: soft, hard, and broad—the broad band being the sum of the soft and hard. We define these bands by a range of channel numbers in a manner convenient to each source. Generally, this range is chosen to maximize the resolution of the detector and the quality of the data while allowing the soft and hard bands an equal representation. Toward this end we avoid channels of low signal-to-noise ratio, which typically occur in the lowest and highest channels; we consistently exclude the first two channels, which have the broadest Gaussian cores; and, to the extent that it is possible, we assign an equal number of counts to each band. This procedure is tailored for comparing an effect for a given source between generally soft and generally hard X-rays, while lacking in a consistent assignment of energies to each band. This definition is, however, more appropriate in light of the IPC's finite energy resolution.

a) Serendipitous Sources

Measuring the SBP is a simple matter of summing counts azimuthally in annular bins centered on the image of each source. Generally, we assume circular symmetry and integrate over all angles. This procedure cannot be followed blindly, however, due to the possibility of including counts from serendipitous X-ray sources in the SBP of the target source. Toward this end, we examined contour plots for each field in search of any indication of serendipitous point sources. This served as a check against the sources discovered by the standard on-line detect algorithms. Half the fields contained one or more secondary sources: four or more sources in the field of Cyg X-3, two in the field of LMC X-1, and one in the field of 4U 1254-69. Since these sources were typically hundreds to thousands of times dimmer than the target source, they could be excluded by restricting the angles from which counts were collected to produce the measured SBP. In all cases, we erred on the side of extreme caution: while the secondary source southwest of 4U 1254-69 could be avoided by omitting a few degrees in one annular bin, we allotted entire quadrants for the sources in the field of Cyg X-3 and LMC X-1. In the case of Cyg X-3, counts were collected from the east and west only to avoid a cluster of sources to the north and a source or two to the south. For LMC X-1, the integration was restricted to the south and east. This avoided two apparent sources in the field as well as two seen more clearly in nearby fields—one of which is blocked by the ribs in this observation, and another which is related to the complex emission of the 30 Doradus region—both of which are to the north of LMC X-1. In sum, we have taken extreme caution to exclude the contributions of serendipitous X-ray sources to the SBP of our target sources. What signal remains should be due entirely to the contribution of the target source.

b) Background Subtraction

Another matter of import is the determination of background. Usually, background is taken as the signal in an annulus centered on the source at some appropriate radial distance. In light of the broad PRF and the extended nature of X-ray halos, this procedure is entirely inappropriate for our purposes. Instead, we have subtracted background by scaling a deep survey field to the same length of time as each of our source observations. In this way, background can be determined in the identical annular regions of the detector as the signal for the source. This allows the SBP of each source to be measured to the very edge of the IPC—independent of any assumptions concerning its real extent—while accounting for the spatial variation of the background across the field.

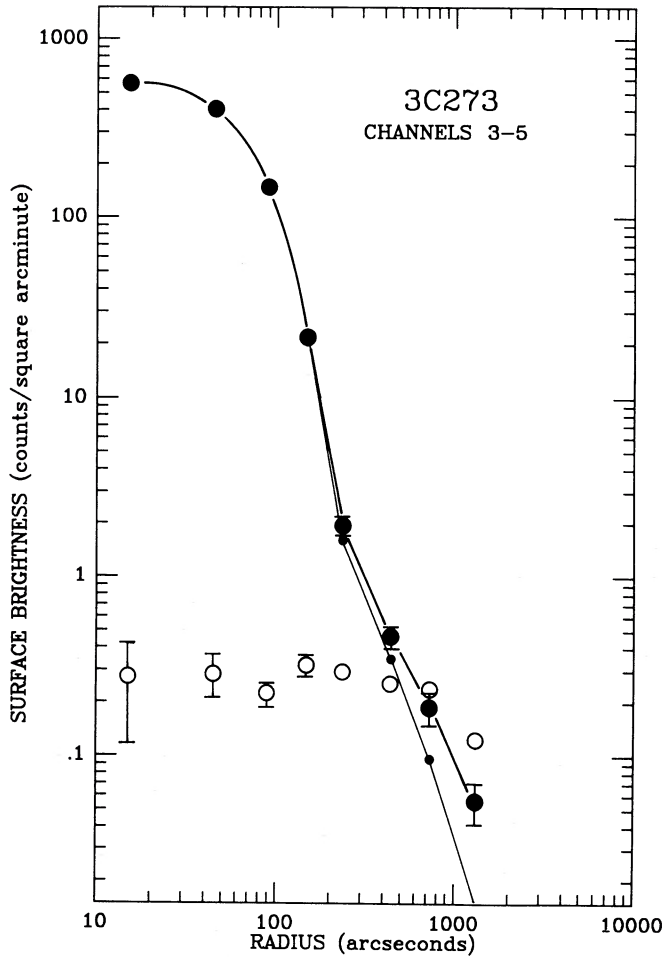


FIG. 4a

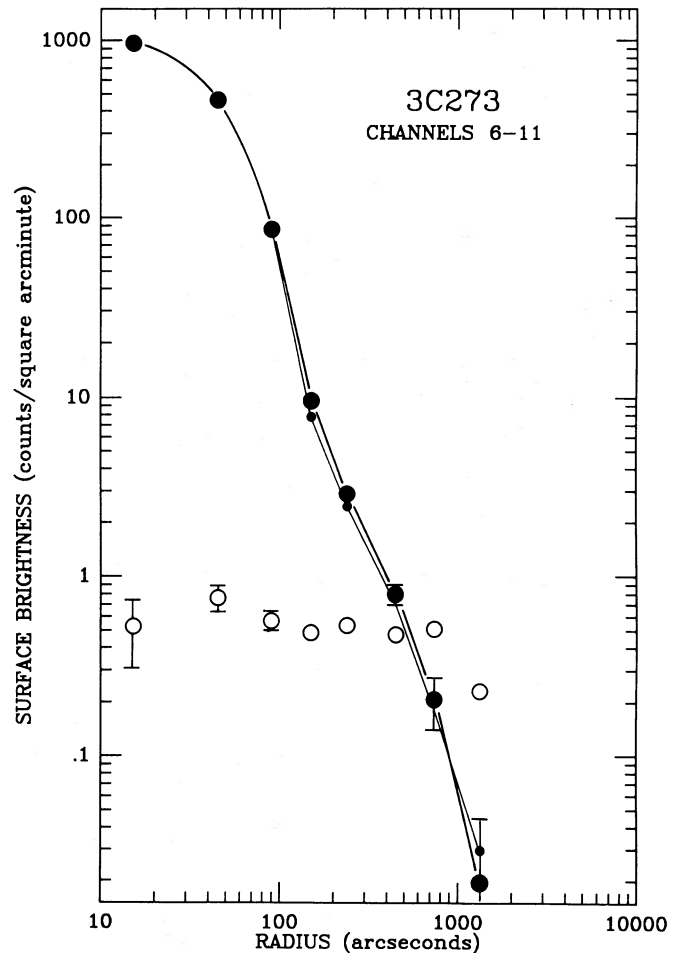


FIG. 4b

FIG. 4.—The measured and model surface brightness profiles for 3C 273. The pulse height distribution has been cut down the middle to produce separate profiles for (a) soft and (b) hard channels. The data are in heavy lines and large filled circles; the model in light lines and small circles; the background is indicated by open circles. The binning is 0', 0.5', 1', 2', 3', 5', 10', 15', and 30', and the error bars for the measured quantities are shown whenever they are larger than the points.

It should be noted, however, that this procedure does not account for potential differences in the background rates between two observations due to variations in the background, which is the net result of a number of independent contributions, some of which are temporally variable, and some of which are to a large degree constant in time. The major contribution to the latter component is due to the diffuse X-ray background and to the leakage of the IPC's calibration source. The largest contribution to the temporally varying component of the background is due to cosmic rays, to charged particles trapped in Earth's magnetic field, and to solar X-rays, which enter the telescope after scattering from the sunlit Earth. This latter temporal component is determined by the amount of solar activity and by the viewing geometry of the satellite, whereas the charged particle flux varies with the amount of solar activity and with the position of the satellite in its orbit. Because of these effects, we have limited our source observations to intervals during which both the viewing geometry and the charged particle rates were favorable.³ These precautions limit the error in our determination of the background to $\sim 10\%$. Accordingly, we have included a systematic error of 10% with the statistical errors associated with the counts in the deep survey fields in our estimate of the source background.

VI. MODEL VERSUS MEASURED PROFILES

The measured SBPs are compared to the model profiles in Figures 4–9. A significant excess surface brightness above the model profiles is apparent for the Galactic (low-latitude) sources. This contrasts with the insignificant excess for the extragalactic (high-latitude) sources 3C 273 and LMC X-1. Four properties of this excess surface brightness unmistakably identify it as the signature of X-ray scattering from interstellar grains:

1. The magnitude of the excess is larger in the soft than in the hard energy band. This behavior is expected for an X-ray halo, due to the E^{-2} energy dependence in the scattering cross section.

³ Furthermore, the effect of these temporal background components has been lessened to some degree by our exclusion of the first two pulse height channels (on the basis of their poor spatial resolution), since these components of the background manifest themselves most prominently in the lowest pulse height channels.

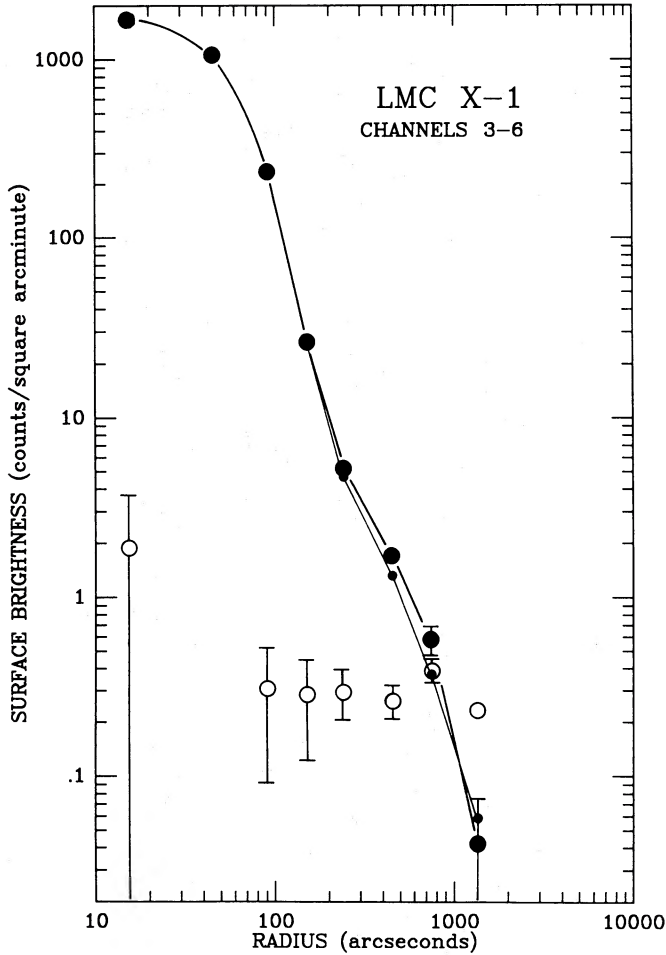


FIG. 5a

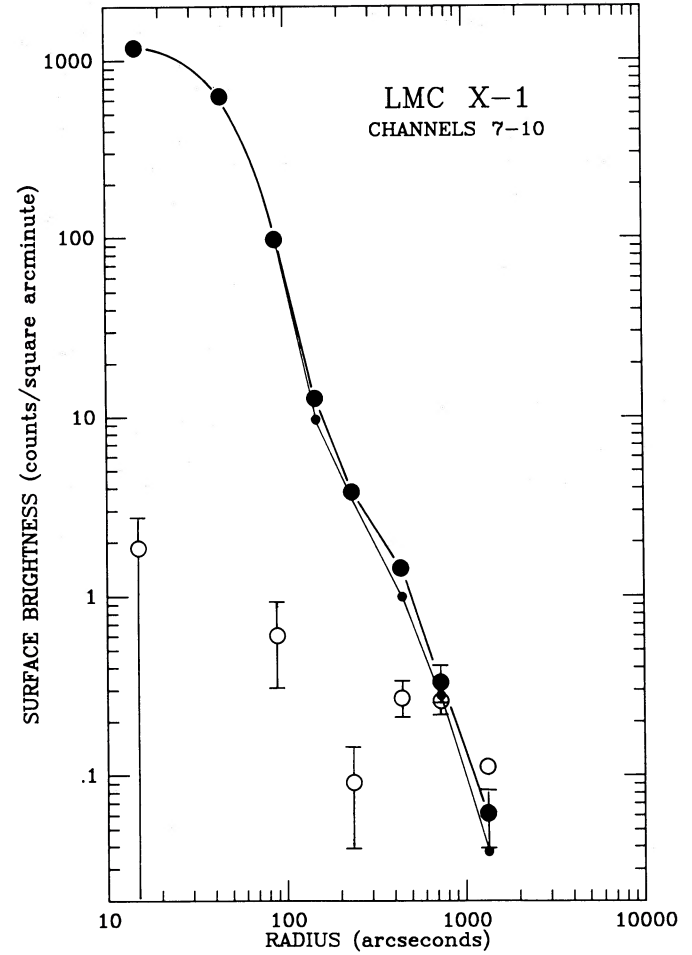


FIG. 5b

FIG. 5.—Similar to Fig. 4, for LMC X-1

2. The magnitude of the excess (which, by eq. [14], is $\sim \sigma_{\text{scat}} n_g d$) correlates well with (a) the number of magnitudes of visual extinction and (b) the distance through the Galaxy's dust layer: quantities which measure the column density of grains to a given source. The data for this correlation appear in Table 2 and are plotted in Figure 10.⁴

3. The magnitude of this excess implies reasonable grain parameters. Using the data from Table 2 for Cyg X-3, for example: $d \approx 10$ kpc and $\sigma_{\text{scat}} n_g d \langle E^* \rangle^2 = 0.178$, we find

$$n_g \sigma_{\text{scat}} \approx 0.18 \text{ kpc}^{-1} \text{ at } 1 \text{ keV}, \quad (21)$$

just as was predicted by equation (15). Consequently,

$$\sigma_{\text{scat}} \approx 5.8 \times 10^{-11} \left(\frac{10^{-12}}{n_g} \right) \text{ cm}^2, \quad (22)$$

implying a mean grain size

$$a \approx 0.098 \left(\frac{2Z}{M} \right)^{-1/2} \left(\frac{\rho}{3} \right)^{-1/2} \left(\frac{10^{-12}}{n_g} \right)^{1/4} E(\text{keV})^{1/2} \left[\frac{F(E)}{Z} \right]^{-1/2} \mu\text{m} \approx 0.1 \mu\text{m}. \quad (23)$$

4. Lastly, as we will show in the next section, the shape of the observed excess surface brightness agrees well with the shape of model halos produced by a Monte Carlo code (cf. Fig. 11).

VII. GRAIN DISTRIBUTIONS AFFECTING THE SHAPE OF AN X-RAY HALO

An analysis of the size and shape of these X-ray halos is a difficult matter, due to the fact that we measure the distribution of angular displacements $I(\theta_{\text{meas}})$ of scattered rays in the size and shape of a halo and not the differential cross section $I(\theta_{\text{scat}})$ (given by

⁴ In light of the discussion in § IIa concerning the energy dependence of the scattering cross section, we point out that the tight correlation implied by the straight line in that figure must be largely fortuitous.

eq. [10]). These two distributions are related by $\theta_{\text{meas}} = (1 - x)\theta_{\text{scat}}$, where x is the fractional distance to the X-ray source: $0 \leq x \leq 1$. In general, the shape of a halo is the sum of contributions from all x :

$$I(\theta_{\text{meas}}) \propto \int_0^1 f(x) \exp[-\theta_{\text{meas}}^2/2(1-x)^2\tilde{\sigma}^2] dx, \tag{24}$$

where $f(x)$ is the spatial distribution of grains along the line sight.

This functional form allows us to investigate the behavior of $I(\theta_{\text{meas}})$ as a function of $f(x)$. As an example, consider the following simple distributions:

1. For the case of N thin scattering screens, $f(x) = \sum_{i=1}^N \delta(x - x_i)$,

$$I(\theta_{\text{meas}}) \propto \sum_{i=1}^N \exp[-\theta_{\text{meas}}^2/2(1-x_i)^2\tilde{\sigma}^2], \tag{25}$$

the halo is the sum of N Gaussians with widths $(1 - x_i)\tilde{\sigma}$. Consequently, the halo from a thin screen of dust midway between the source and the observer is Gaussian in shape and has a width $\frac{1}{2}\tilde{\sigma}$; the halo from dust at $x = 1 - \epsilon$ (very near the source) has a width $\epsilon\tilde{\sigma}$; the halo from dust at $x = \epsilon$ (very near the observer) has a width $\tilde{\sigma}$; and so on. The halo for LMC X-1, for instance, has two components: one broad, due to scattering in our own Galaxy, and another narrow (and consequently unobservable), due to scattering in the Large Magellanic Cloud.

2. For the case of a uniform spatial distribution, $f(x) = \text{constant}$,

$$I(\theta_{\text{meas}}) \propto \int_0^1 \exp[-\theta_{\text{meas}}^2/2(1-x)^2\tilde{\sigma}^2] dx, \tag{26}$$

which is the incomplete gamma function $\Gamma(-\frac{1}{2}, \theta_{\text{meas}}^2/2\tilde{\sigma}^2)$.

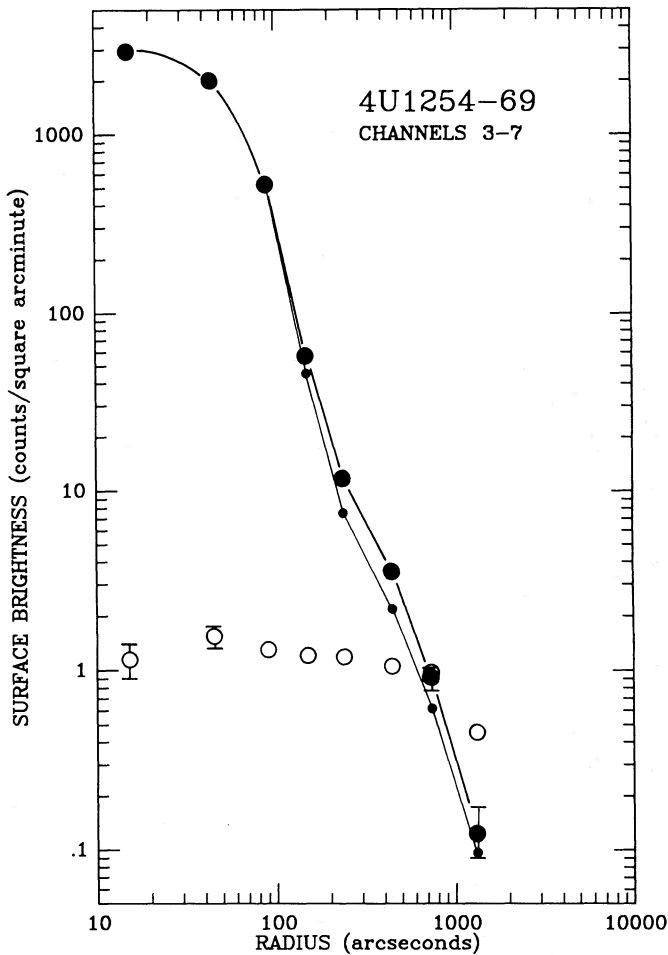


FIG. 6a

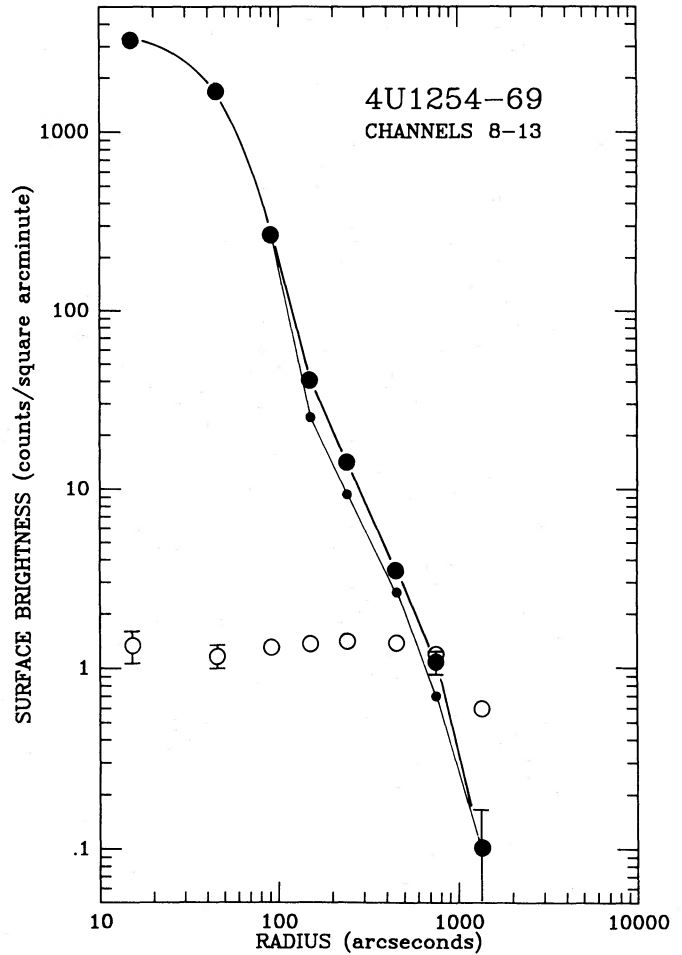


FIG. 6b

FIG. 6.—Similar to Fig. 4, for 4U 1254 - 69

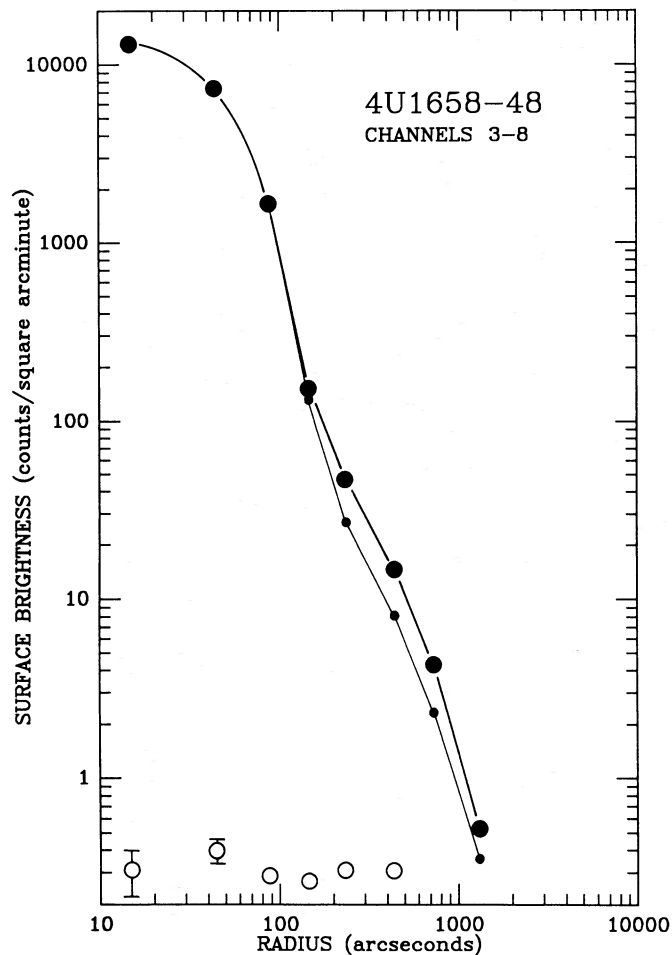


FIG. 7a

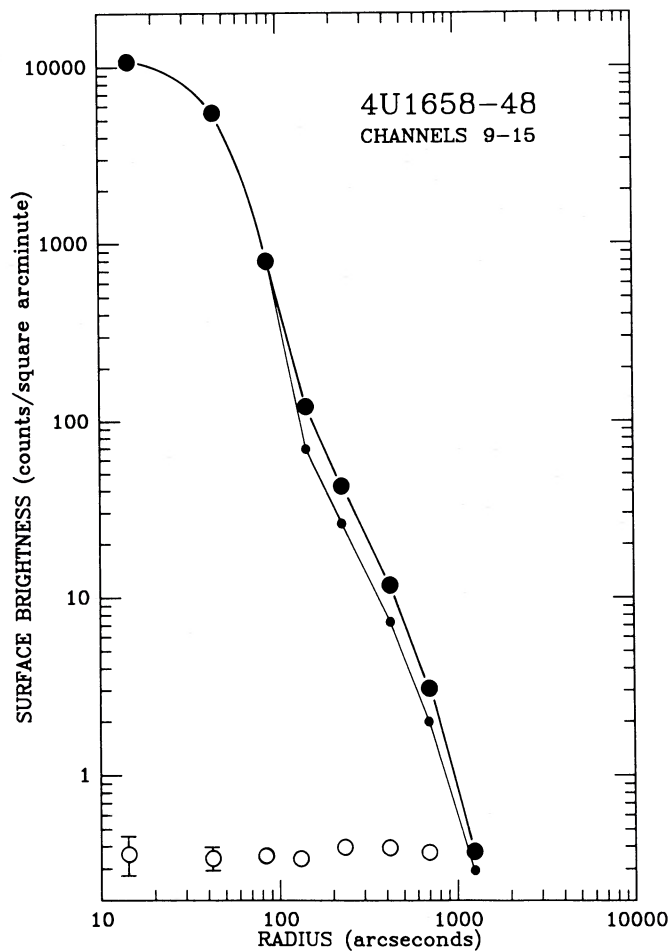


FIG. 7b

FIG. 7.—Similar to Fig. 4, for 4U 1658–48

Note that these results are for constant $\tilde{\sigma}$. Due to the dependence of $\tilde{\sigma}$ on E and a (through eq. [6]), these results must as well be integrated over (1) the particle size distribution $n(a)$ and (2) the source spectrum, to obtain the form for a given source's X-ray halo. Clearly, this is a formidable analytic task, even for such a simple spatial distribution as is illustrated in the second example above. Because of these complications, we have chosen to evaluate this integral numerically for various grain distributions $f(x)$ and $n(a)$ by means of a Monte Carlo code.

A complication of this Monte Carlo procedure in its simplest form is that it is restricted to single energies, due to the energy dependence of σ_{scat} and $\tilde{\sigma}$, and thereby to the construction of monoenergetic halos. However, the halo for a given source may be constructed from a number of monoenergetic halos, just as the SBP for a given source was constructed from a number of monoenergetic PRFs. This separate accounting of the halos at different energies allows us also to account for the effect of the IPC/mirror PRF on the true surface brightness of the model halos.

VIII. GRAIN SIZE DISTRIBUTIONS

Having designed a procedure by which halos may be constructed for a given source for given grain parameters, we are now in a position to compare the model halos to the observed halos and thereby investigate the forms allowed to the grain distributions. In order to evaluate the size distribution $n(a)$ alone, we have assumed the spatial distribution $f(x)$ to obey a simple model: the density of grains is taken to be uniform in planes parallel to the Galaxy's disk and to decrease exponentially with the distance z above the Galactic plane with a scale height z_0 of 100 parsecs:

$$f(x) = n_0 \exp(-z/z_0) = n_0 \exp[-10D(\text{kpc}) \sin(b)x], \quad (27)$$

where $D(\text{kpc})$ is the distance to the source in kiloparsecs, and b is its Galactic latitude. The following results are not particularly sensitive to this assumption, which was made in analogy with the distribution of gas in the Galaxy. The scale height of 100 pc produces the correct effective thickness of the Galaxy's dust layer (Spitzer 1978). With this function fixed, the (unconvolved, single

energy, single size) halo

$$I(\theta_{\text{meas}}) \propto \int_0^1 n_0 \exp[-10D(\text{kpc}) \sin(b)x] \exp[-\theta_{\text{meas}}^2/2(1-x)^2\bar{\sigma}^2] dx, \quad (28)$$

which is evaluated by the numerical method previously described.

The grain size distributions which we have investigated are of three forms:

1. a single size "distribution": $n(a) \propto \delta(a - a_i)$;
 2. a Mathis-Rumpl-Nordsieck (1977, hereafter MRN) distribution: $n(a) \propto a^{-q}$ for $a_- \leq a \leq a_+$; and
 3. an Oort-van de Hulst (1946, hereafter OVH) distribution, as parameterized by Greenberg (1966): $n(a) \propto \exp[-5(a/a_i)^3]$;
- each of which enters into the integral weighted toward large grain radii by the size dependence of the total scattering cross section: as $a^4 n(a)$. Because of this, an MRN distribution enters as a^{4-q} and produces equal contributions from all sizes for $q = 4$, whereas an OVH distribution enters as $a^4 \exp[-5(a/a_i)^3]$, which is strongly peaked about $0.64a_i$.

IX. GRAIN PARAMETERS

The most striking result of our investigation is that no single grain size is capable of producing the observed halos. Single-sized halos are fairly flat at small angles and drop off steeply at large angles—a behavior which is not seen in the data (cf. Fig. 11). Because of the contribution to our sources' halos at both small and large angles, some distribution of sizes from large to small is required. We find that either of the two size distributions is capable of reproducing the observed halos, although an MRN distribution formally produces better fits to the data in every case. This is not entirely surprising, however, since the MRN distribution has three times as many free parameters as the OVH distribution. Better fits could probably be obtained with the latter with as many free parameters: for instance, with a two-component mixture,

$$n(a) \propto \exp[-5(a/a_i)^3] + n \exp[-5(a/a_j)^3], \quad (29)$$

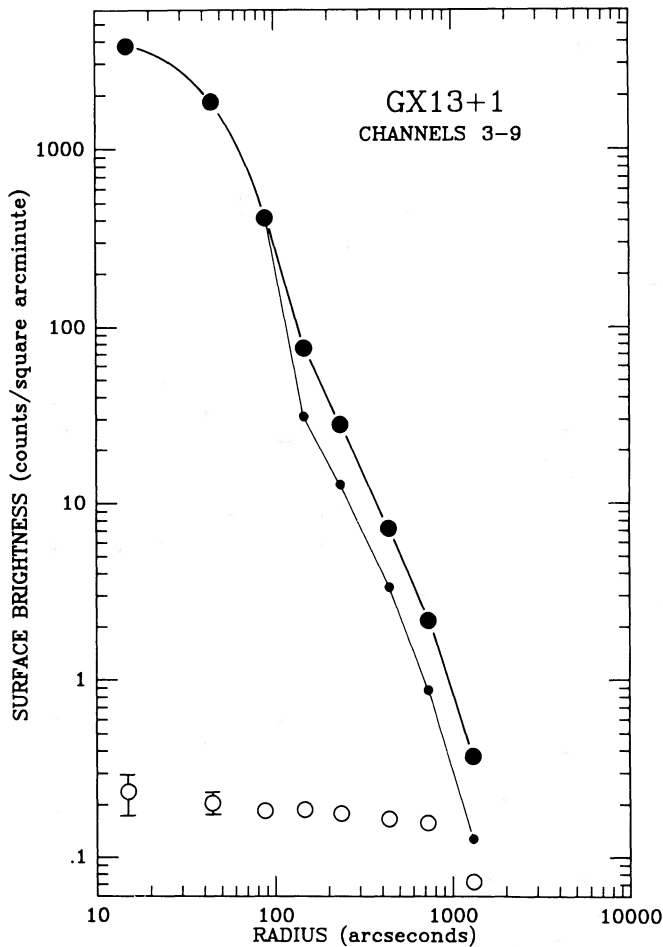


FIG. 8a

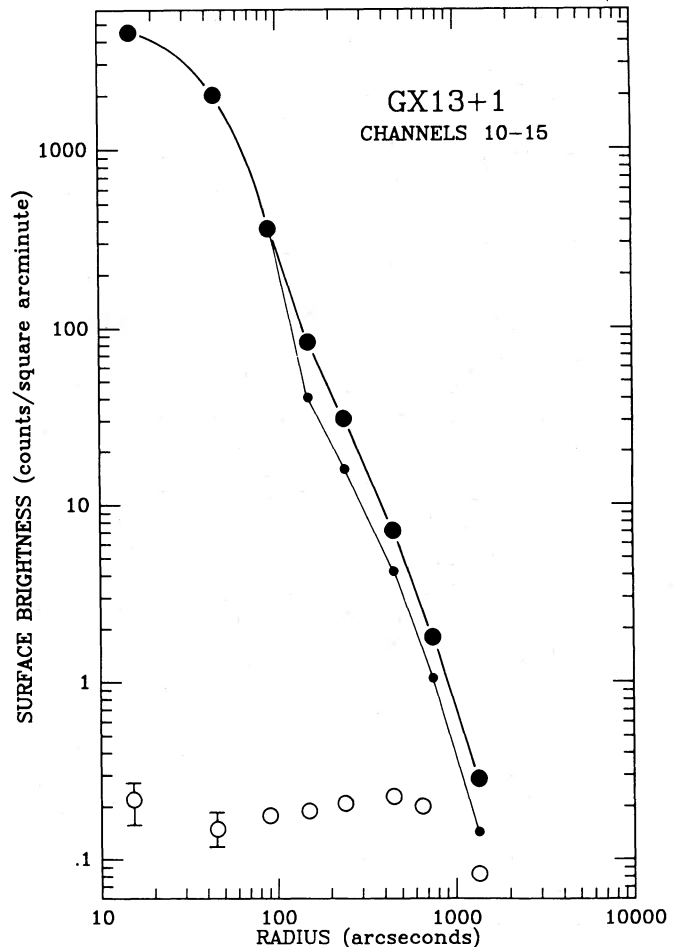


FIG. 8b

FIG. 8.—Similar to Fig. 4, for GX 13+1

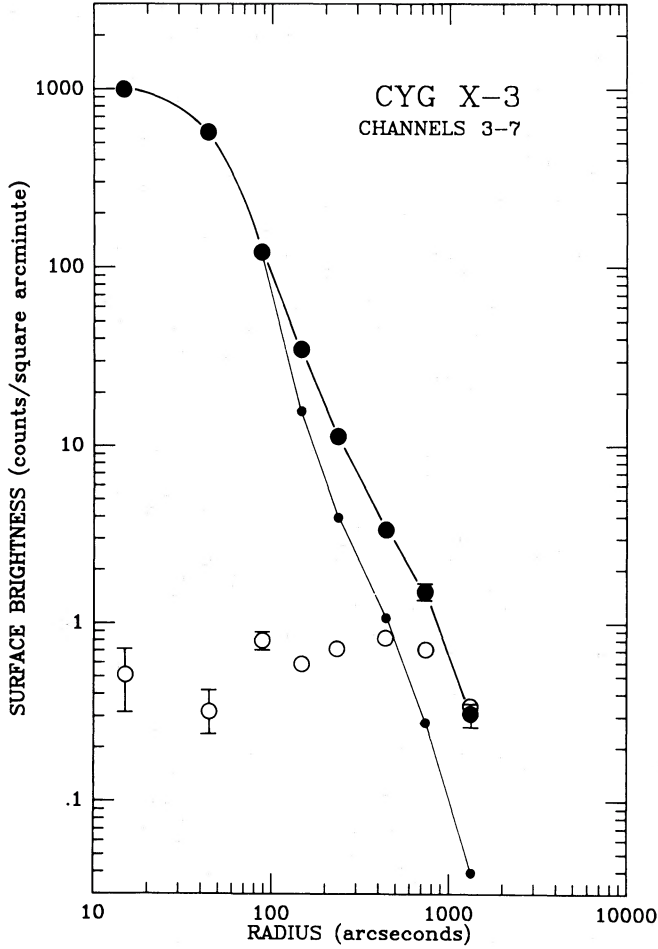


FIG. 9a

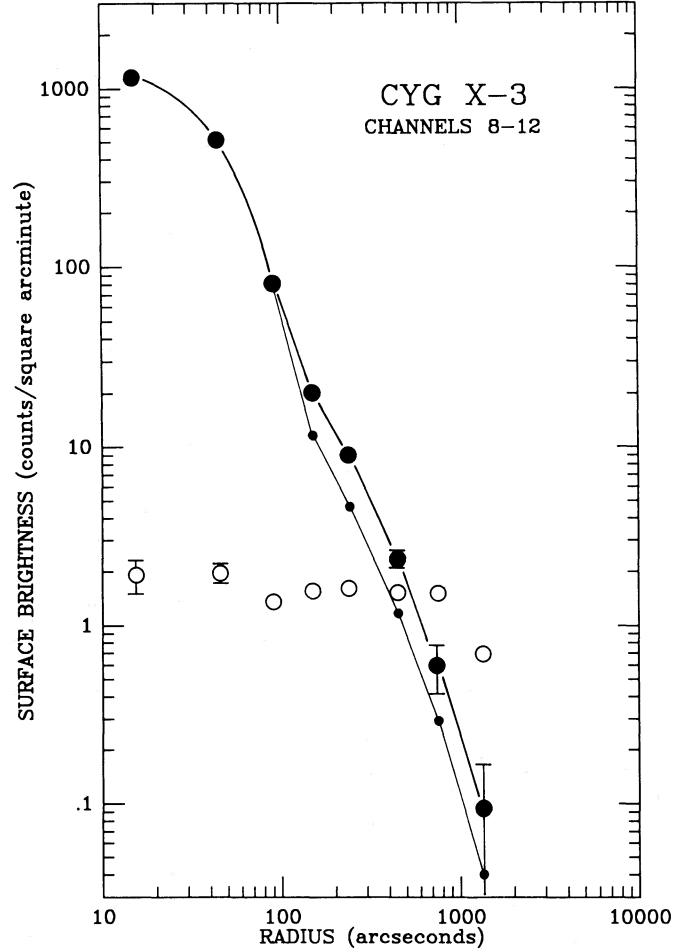


FIG. 9b

FIG. 9.—Similar to Fig. 4, for Cyg X-3

where n is proportional to the relative number density of the constituents i and j : (n_i/n_j). Because of this, we find no compelling reason to choose one distribution over the other.

For an MRN distribution, an index of $q \approx 3.5$ – 4.5 is indicated, with a lower cutoff of nearly zero, $a_- \approx 0.0$ – $0.03 \mu\text{m}$, and an upper cutoff $a_+ \approx 0.2$ – $0.3 \mu\text{m}$. This corresponds well with the range of sizes and power-law values found by MRN for the “silicate” component of a two-component mixture, which was constructed to match the wavelength dependence of the interstellar extinction. This mixture is composed of graphite grains with sizes $0.005 \lesssim a \lesssim 1 \mu\text{m}$ and $q \approx 3.3$ – 3.6 , and another material (a “silicate”: enstatite, olivine, silicon carbide, iron, and magnetite were considered) with sizes $0.025 \lesssim a \lesssim 0.25 \mu\text{m}$ and the same index. In practice, this distribution is applied with a large-size cutoff $a_+ \approx 0.25 \mu\text{m}$ for both components (Mathis and Wallenhorst 1981; Draine and Lee 1984, hereafter DL), though it would not be surprising if we picked out the range of sizes of this more general two-component mixture where the constituents overlap. Of interest in this matter as well is the finding by Bode *et al.* 1985 that the X-ray halo of Cyg X-1 could be fitted well with an upper cutoff $0.15 \lesssim a_+ \lesssim 0.25 \mu\text{m}$.

For an OVH distribution, the characteristic size indicated by our models is in the range $a_i \approx 0.1$ – $0.2 \mu\text{m}$. This result is not inconsistent with the sizes generally ascribed to this distribution, as, for instance, for “silicates” and graphite (Greenberg and Hong 1975), and for “ices” (Greenberg, van de Bult, and Allamandola 1983). The characteristic size we derive most likely refers to the former constituents, however, since the density dependence of the total scattering cross section enhances the effect of the graphite and “silicate” grains with respect to the low-density “ice” grains.

These results have one important and immediate application: in terms of these models, the average grain size

$$\langle a \rangle = \int a \sigma_{\text{scat}}(a) dn(a) / \int \sigma_{\text{scat}}(a) dn(a) \approx \left(\frac{5-q}{6-q} \right) a_+ \quad \text{and} \quad 0.65 a_i \quad (30)$$

for the MRN and OVH distributions respectively. Consequently, $\langle a \rangle \approx 0.1 \mu\text{m}$ for either distribution, given the values we have found for q , a_+ , and a_i from the shapes of the X-ray halos. This is just the value of the mean grain size derived independently from the magnitude of the halo intensity as a function of distance (see Fig. 10 and eqs. [21]–[23]). This internal consistency between

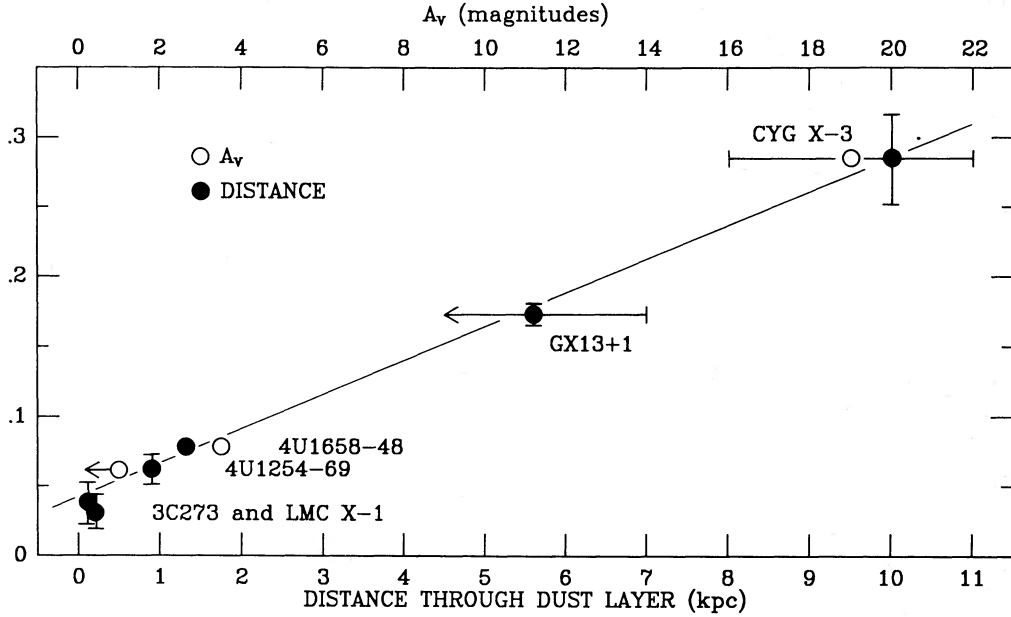


FIG. 10.—Correlation between the fractional halo intensity and (1) the number of magnitudes of visual extinction and (2) the distance to each source through the Galaxy's dust layer, which is taken as a disk with half-thickness 100 pc; for sources out of the plane, $d(\text{kpc}) = 0.1/\sin b$, where b is the source's Galactic latitude. The line (which is simply fitted by eye) is drawn to emphasize the extent of the correlation.

parameters derived from two entirely different halo properties—their shape and their strength—is a striking piece of evidence supporting our interpretation and analysis of these data.

Another parameter derivable from our measurements relates to the grain number density. After DL, we write

$$dn_i(a) = A_i n_H a^{-a} da \quad \text{for} \quad a_- \lesssim a \lesssim a_+ \quad (31)$$

for the number density of grains of each type i with radii in the interval $[a, a + da]$. (In what follows, the subscript is omitted for the sake of simplicity.) The value of A can be obtained from the integral

$$\int \sigma_{\text{scat}}(a) dn(a) = n_g \sigma_{\text{scat}}, \quad (32)$$

TABLE 2
SOURCE INFORMATION

Source	l	b	A_i^a (mag)	d (kpc)	Fractional Halo Intensity ^b	$\sigma_{\text{scat}} n_g d^c$	$\langle E \rangle^d$ (keV)	$\langle E^* \rangle^e$ (keV)	$\sigma_{\text{scat}}^* n_g d^f$
3C 273	290°	+64.5	...	0.11 ^g	0.04 ± 0.02	0.04 ± 0.02	0.50	0.22	0.002 ± 0.001
LMC X-1	280	+31.5	...	0.19 ^g	0.03 ± 0.01	0.03 ± 0.01	1.67	1.37	0.06 ± 0.02
4U 1254-69	304	-6.4	<1	0.90 ^g	0.06 ± 0.01	0.06 ± 0.01	1.51	1.07	0.07 ± 0.01
4U 1658-48	339	-4.3	3.5	1.33 ^g	0.078 ± 0.003 ^h	0.081 ± 0.003	1.55	1.28	0.133 ± 0.005
GX 13+1	13.5	+0.1	?	<5.6 ⁱ	0.17 ± 0.01 ^j	0.19 ± 0.01	2.42	2.13	0.85 ± 0.05
Cyg X-3	79.9	+0.7	19	10 ^{-1/2} ^k	0.28 ± 0.03	0.33 ± 0.05	2.72	2.31	1.78 ± 0.25

^a Bradt and McClintock 1983.

^b $I_{\text{Halo}}/(I_{\text{Halo}} + I_{\text{Core}}) = (I_{\text{Meas.}} - I_{\text{Model}})/I_{\text{Meas.}}$ beyond 2'. The contribution interior to this radius is model-dependent, but is typically a few (\lesssim) 5 percent.

^c From eq. (14), the "optical" depth $\sigma_{\text{scat}} n_g d = -\ln(1 - \text{fractional halo intensity})$.

^d $\langle E \rangle = \int EN(E)dE / \int N(E)dE$ is the average photon energy, where $N(E)$ is the photon number spectrum for each of the source spectra listed in Table 1.

^e $\langle E^* \rangle = \int E \sigma_{\text{scat}} N(E)dE / \int \sigma_{\text{scat}} N(E)dE$ is the average photon energy weighted by the total scattering cross section.

^f The "optical" depth $\sigma_{\text{scat}} n_g d$ evaluated at 1 keV, obtained by use of eq. (11): $\sigma_{\text{scat}}^* n_g d = \sigma_{\text{scat}} n_g d \langle E^* \rangle^2$.

^g Distance through a dust layer of half-thickness 100 pc: $d(\text{kpc}) = 0.1/\sin b$, such that the column density of grains $N_g = n_g d$ for each source.

^h To be compared to the early IPC result of Rolf 1983: 0.05–0.09.

ⁱ Distance based on the unabsorbed flux and an assumed X-ray luminosity $L_X = L_{\text{Edd}} = 10^{38}$ ergs s⁻¹.

^j To be compared to the HRI result of Catura 1983: 0.18 ± 0.02.

^k From Bradt and McClintock 1983. The value of $d \gtrsim 11.6$ kpc found by Dickey (1983) is not applicable, since this source breaks out of the Galaxy's dust layer at $d \approx 8$ kpc, given that its Galactic latitude $b \approx 0.7$.

which we found to be approximately equal to 0.18 kpc^{-1} (eq. [21]). Consequently,

$$6.3 \times 10^9 A n_{\text{H}} \left(\frac{2Z}{M} \right)^2 \left(\frac{\rho}{3} \right)^2 E(\text{keV})^{-2} \left[\frac{F(E)}{Z} \right]^2 \int_{a_-}^{a_+} a^{4-q} da \approx 5.8 \times 10^{-23} \text{ cm}^{-1}. \quad (33)$$

The integral is equal to $a_+^{5-q}/(5-q)$ to sufficient accuracy, and so

$$A \approx 9.2 \times 10^{-33} \left(\frac{5-q}{a_+^{5-q}} \right) n_{\text{H}}^{-1} \left(\frac{2Z}{M} \right)^{-2} \left(\frac{\rho}{3} \right)^{-2} E(\text{keV})^2 \left[\frac{F(E)}{Z} \right]^{-2}, \quad (34)$$

which unfortunately spans a range of values in excess of 10^5 , given the range of values to which we have been able to restrict the parameters a_+ and q . Using the MRN values ($a_+ = 0.25 \mu\text{m}$, $q = 3.5$), however,

$$\log A \approx -24.96 + \log \left\{ n_{\text{H}}^{-1} \left(\frac{2Z}{M} \right)^{-2} \left(\frac{\rho}{3} \right)^{-2} E(\text{keV})^2 \left[\frac{F(E)}{Z} \right]^{-2} \right\}, \quad (35)$$

where A is in units of $\text{cm}^{2.5}$. If this is interpreted as being the sum of equal contributions from the graphite and "silicate" components,

$$\log A_i \approx -25.26, \quad (36)$$

in excellent agreement with the values reported by MRN and DL:

$$\log A_{\text{silicate}} = -25.24, \quad \log A_{\text{graphite}} = -25.21$$

and

$$\log A_{\text{silicate}} = -25.07, \quad \log A_{\text{graphite}} = -25.13 \quad (37)$$

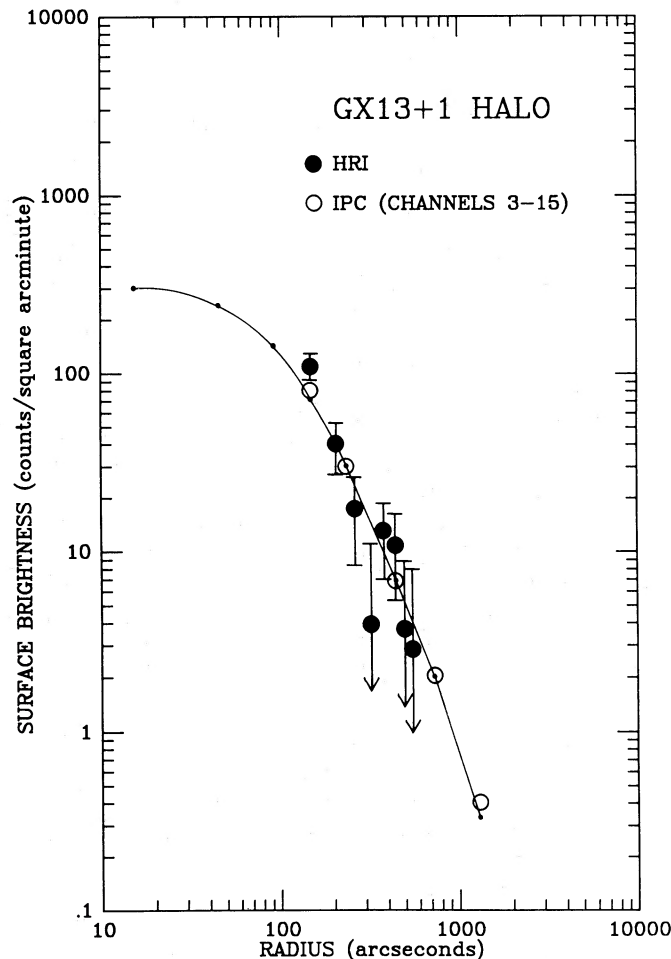


FIG. 11.—The X-ray halo for GX 13+1. The points for the IPC are taken from the difference between the measured and model profiles in Fig. 8; the HRI points are from Fig. 4 of Catura (1983) (with arbitrary normalization). The best-fit absolute surface brightness model halo (which incorporates the IPC's spatial resolution) for the IPC data is drawn in light lines. The halos for 4U 1658-48 (Fig. 7) and Cyg X-3 (Fig. 9) are very similar.

respectively. For “silicate” grains in the form of olivine $[\text{Mg}_{1.1}\text{Fe}_{0.9}\text{SiO}_4]$ with $\rho = 3.3 \text{ g cm}^{-3}$, and graphite grains with $\rho = 2.3 \text{ g cm}^{-3}$, this result confirms the MRN and DL finding that essentially all the silicon, magnesium, and iron (though little of the oxygen), and $\sim 60\%$ of the carbon is locked up in the form of grains: results which are in general agreement with the observed depletion of these elements from the gas phase of the interstellar medium (Spitzer and Jenkins 1975).

The corresponding relations to equations (31) and (35) for the OVH distribution are

$$dn_i(a) = B_i n_H \exp[-5(a/a_i)^3] da \quad (38)$$

and

$$\log B \approx -6.23 - 5 \log [a_i(0.15 \mu\text{m})] + \log \left\{ n_H^{-1} \left(\frac{2Z}{M} \right)^{-2} \left(\frac{\rho}{3} \right)^{-2} E(\text{keV})^2 \left[\frac{F(E)}{Z} \right]^{-2} \right\}, \quad (39)$$

where B is in units of cm^{-1} . If, as for the MRN grains, we take this to be the sum of equal contributions from graphite and “silicate” components,

$$\log B_i \approx -6.53, \quad (40)$$

which exhausts $\gtrsim 80\%$ of the available silicon, magnesium, and iron (if the “silicate” grains are in the form of olivine), and $\sim 60\%$ of the available carbon—just as was found for the MRN mixture.

A related parameter is the total grain number density, n_g . From the integral of equation (31),

$$n_g \approx A n_H a_-^{1-q} / (q-1), \quad (41)$$

to sufficient accuracy. Using the value of A from equation (34),

$$n_g \approx 9.2 \times 10^{-33} \left(\frac{5-q}{q-1} \right) \frac{a_-^{1-q}}{a_+^{5-q}}, \quad (42)$$

which is extremely poorly determined due largely to the uncertainty in the value of the lower size cutoff. Using the MRN values ($q = 3.5$, $a_+ = 0.25 \mu\text{m}$, and $a_- = 0.025 \mu\text{m}$), however,

$$n_g \approx 4.5 \times 10^{-12} \text{ cm}^{-3}, \quad (43)$$

while the corresponding quantity for the OVH distribution is

$$n_g \approx 4.6 \times 10^{-12} a_i(0.15 \mu\text{m})^{-4} \text{ cm}^{-3}, \quad (44)$$

both of which are to order of magnitude consistent with the scaling we have been using for n_g .

X. SUMMARY

The most general result of our and Catura's (1983) investigation is that halos produced by the scattering of X-rays from interstellar grains are a feature endemic to Galactic X-ray sources. We find in this study that in every respect the grains responsible for this scattering are identical to the grains responsible for optical extinction. In particular, we find that the intensity of the halos is consistent with a mean size $\sim 0.1 \mu\text{m}$ and a number density $\sim 10^{-12} \text{ grains cm}^{-3}$. Moreover, a wide range of sizes is required to explain the size and shape of the halos. In the context of the MRN size distribution, this is given by a power law of index $q \approx 3.5\text{--}4.5$ with upper and lower cutoffs $a_+ \approx 0.2\text{--}0.3 \mu\text{m}$ and $a_- \approx 0.0\text{--}0.03 \mu\text{m}$ respectively. For the OVH distribution, $a_i \approx 0.1\text{--}0.2 \mu\text{m}$. From these parameters, and from the intensity of the halos as a function of distance through the Galaxy's dust layer, we find that the amount of material in grains is in general agreement with the observed depletion of the elements from the gas phase of the interstellar medium. Specifically, our results are consistent with a multicomponent mixture of large mass number “silicates” and graphite, with sufficient number to essentially exhaust the available amount of heavy elements and $\sim 60\%$ of the cosmic abundance of carbon respectively. Importantly, these findings are in detailed agreement with the specific predictions of the MRN size distribution, which was constructed to match the wavelength dependence of the interstellar extinction.

With the knowledge gained from this study of a number of point X-ray sources, and with the understanding that halos are to be found around all distant Galactic X-ray sources, we have undertaken an examination of the surface brightness profiles of the brightest Galactic supernova remnants imaged by the *Einstein Observatory* (Mauche and Gorenstein 1985a, b). Although details concerning this work must await a future publication by the present authors, we note here that each of these sources have halos consistent with X-ray scattering from interstellar grains.

Future imaging observations of X-ray halos offer promising refinements of the grain parameters derived in this paper, particularly in light of the potential reduction in the amount of mirror scattering offered by the next generation of X-ray mirrors. The enhanced energy resolution of the latest imaging detectors will as well allow a detailed investigation of the elemental composition of interstellar grains (Martin and Sciama 1970; Martin 1970), which relies on a comparison of the intensity of a source's halo on either side of an absorption edge. With these studies, and with the constraints imposed by the wavelength dependence of the interstellar extinction, as well as with the observed depletion of the elements from the gas phase of the interstellar medium, it should be possible in the near future to uniquely define the nature of interstellar grains.

The authors are happy to acknowledge the invaluable assistance of D. Fabricant in the initial stages of this project. We are grateful for the help of L. Van Speybroeck, R. Harnden, J. McSweeney, and the members of the data support staff. Thanks are due to G. Field, J. Grindlay, J. Mathis, L. Molnar, J. Raymond, and an anonymous referee for reading and commenting on a preliminary version of this manuscript. This work was supported by NASA contract NAS8-30751.

REFERENCES

- Alcock, C., and Hatchett, S. 1978, *Ap. J.*, **222**, 456.
 Bode, M. F., Priedhorsky, W. C., Norwell, G. A., and Evans, A. 1985, *Ap. J.*, **299**, 845.
 Bradt, H. V. D., and McClintock, J. E. 1983, *Ann. Rev. Astr. Ap.*, **21**, 13.
 Catura, R. C. 1983, *Ap. J.*, **275**, 645.
 Dickey, J. M. 1983, *Ap. J. (Letters)*, **273**, L71.
 Draine, B. T., Lee, H. M. 1984, *Ap. J.*, **285**, 89 (DL).
 Giacconi, R., et al. 1979, *Ap. J.*, **230**, 540.
 Greenberg, J. M. 1966, in *IAU Symposium No. 24, Spectral Classification and Multicolour Photometry*, ed. K. Lóden, L. O. Lóden, and U. Sinnerstad (London: Academic), p. 291.
 Greenberg, J. M., and Hong, S. S. 1975, in *The Dusty Universe*, ed. G. B. Field and A. G. W. Cameron (New York: Watson), p. 132.
 Greenberg, J. M., van de Bult, C. E. P. M., and Allamandola, L. J. 1983, *J. Phys. Chem.*, **87**, 4243.
 Hayakawa, S. 1970, *Progr. Theor. Phys.*, **43**, 1224.
 Henke, B. L. 1981, in *Low Energy X-Ray Diagnostics*, ed. D. T. Attwood and B. L. Henke (New York: AIP), p. 146.
 Lampton, M., Margon, B., and Bowyer, S. 1976, *Ap. J.*, **208**, 177.
 Martin, P. G. 1970, *M.N.R.A.S.*, **149**, 221.
 Martin, P. G., and Sciama, D. W. 1970, *Ap. Letters*, **5**, 193.
 Mathis, J. S., Rumpl, W., Nordsieck, K. H. 1977, *Ap. J.*, **217**, 425 (MRN).
 Mathis, J. S., and Wallenhorst, S. G. 1981, *Ap. J.*, **244**, 483.
 Mauche, C. W., and Gorenstein, P. 1985a, in *The Crab Nebula and Related Supernova Remnants*, ed. R. B. C. Henry and M. C. Kafatos (Cambridge: Cambridge University Press), p. 81.
 ———. 1985b, *Bull. AAS*, **16**, 926.
 Oort, J. H., and van de Hulst, H. C. 1946, *Bull. Astron. Inst. Netherlands*, **10**, 187 (OVH).
 Overbeck, J. W. 1965, *Ap. J.*, **141**, 864.
 Rolf, D. P. 1983, *Nature*, **302**, 46.
 Spiegelhauer, H., and Trümper, J. 1975, *J. British Interplanetary Soc.*, **28**, 319.
 Spitzer, L., and Jenkins, E. B. 1975, *Ann. Rev. Astr. Ap.*, **13**, 133.
 Spitzer, L. 1978, *Physical Processes in the Interstellar Medium* (New York: Wiley).
 Trümper, J., and Schönfelder, V. 1973, *Astr. Ap.*, **25**, 445.
 van de Hulst, H. C. 1957, *Light Scattering by Small Particles* (New York: Dover).
 van der Klis, M., and Bonnet-Biduard, J. M. 1983, *Astr. Ap. Suppl.*, **50**, 129.

Note added on proof.—Subsequent to the submission of this manuscript, the authors have become aware of a preprint by Priedhorsky and Terrell (*Ap. J.*, **301**, in press [1986]) detailing the flux history of Cyg X-3 as measured by the *Vela 5B* and *Ariel 5* satellites. From their Figure 3, it is apparent that our observation of Cyg X-3 (on 1978 December 16) took place at the end of a ~ 40 day interval during which the average flux from Cyg X-3 decreased by $\sim 50\%$. In light of this information and our discussion at the end of § II concerning the effects of source variability, we must consider more closely the possibility that Cyg X-3's long term flux variations have conspired to produce an atypically bright halo at the time of our observation.

A more detailed investigation into the delays experienced by scattered rays shows that the distribution of time delays is approximately an exponential function with an e -folding time

$$\Delta t = 3.8E(2.3 \text{ keV})^{-2}d(10 \text{ kpc})a(0.1 \mu\text{m})^{-2} \text{ days},$$

where 2.3 keV is the appropriate average photon energy for this source (cf. Table 2). Consequently, our sensitivity to Cyg X-3's long-term flux variations is limited to an interval of ~ 4 days previous to our observation. During this time (assuming a linear decrease of 50% in 40 days), this flux evolution would have resulted in a $\sim 20\%$ brighter halo at the time of our observation. Alternatively (since the *Ariel 5* data are too coarsely binned to tell), the average flux from Cyg X-3 may have been essentially constant for four or more days previous to our observation, as Cyg X-3 was settling into—or had already settled into—an extended period of relative flux stability.

Because of these considerations, we caution that our results for Cyg X-3 (and consequently for our results following eq. [32]) may be in error by an additional $\sim 20\%$. Happily, this result does not alter any of our basic conclusions. For future applications, however, we recommend that the entry in Table 2 for the fractional halo intensity of Cyg X-3 be changed to $0.28^{+0.03}_{-0.07}$. Further observations will be required to refine this measurement.

CHRISTOPHER W. MAUCHE and PAUL GORENSTEIN: Harvard-Smithsonian Center for Astrophysics, 60 Garden St., Cambridge, MA 02138